Biomaterials 317 (2025) 123110

Contents lists available at ScienceDirect

Biomaterials

journal homepage: www.elsevier.com/locate/biomaterials

The effect of the foreign body response on drug elution from subdermal delivery systems

Simone Capuani [a], Nathanael Hernandez [a], Jocelyn Nikita Campa-Carranza [a,b], Nicola Di Trani [a], Takuma Yoshikawa [c], Marco Farina [a], Ashley L. Joubert [a], Camden A. Caffey [a], Alessio Simeone [a,d], Seo Won Cho [e], Patrick S. Stayton [c], Corrine Ying Xuan Chua [a], Alessandro Grattoni [a,f,g,*]

[a] Department of Nanomedicine, Houston Methodist Research Institute, Houston, TX, USA
[b] School of Medicine and Health Sciences, Tecnologico de Monterrey, Monterrey, NL, Mexico
[c] Department of Bioengineering and Molecular Engineering & Sciences Institute, University of Washington, Seattle, WA, USA
[d] Department of Mechanical and Aerospace Engineering, Politecnico di Torino, Torino, Italy
[e] College of Medicine Texas A&M University, Bryan, Houston, TX, USA
[f] Department of Surgery, Houston Methodist Hospital, Houston, TX, USA
[g] Department of Radiation Oncology, Houston Methodist Hospital, Houston, TX, USA

ARTICLE INFO

Keywords:
Foreign body response
Fibrotic capsule
Implantable devices
Long-acting drug delivery
Molecular transport
Pharmacokinetics

ABSTRACT

Contrasting findings are presented in the literature regarding the influence of foreign body response (FBR) on drug release from implantable drug delivery systems. To this end, here we sought direct evidence of the effect of the fibrotic tissue on subcutaneous drug release from long-acting drug delivery implants. Specifically, we investigated the pharmacokinetic impact of fibrotic encapsulation on a small molecule drug, islatravir (293 Da), and a large protein, IgG (150 kDa), administered via biocompatible implants. First, solid implants fabricated from biocompatible PMMA resin, nylon, and PLA were used to characterize the degree of FBR in rats. Despite initial material-dependent differences in the early FBR phase, the thickness and composition of the fibrotic capsules normalized in the chronic phase of FBR. Ex vivo assessments indicated an increase in the diffusivity of both molecules over time, aligning with a reduction in collagen density within the fibrotic tissue. Subsequently, reservoir-based drug delivery devices, matching the solid implants in size, shape and material, were implanted to study in vivo pharmacokinetics. The study revealed consistent plasma levels of islatravir across different implant materials and a temporary modulation of IgG release from PMMA resin implants during the acute FBR phase. End-point histological analyses confirmed that the localized delivery neither incited inflammation in the surrounding tissue nor did it alter vascularization. This evidence suggests that, while acute FBR may transiently affect the release of larger molecules, in the absence of acute local inflammation, fibrotic encapsulation does not significantly impact the steady-state release of small molecule drugs from long-acting implantable delivery systems.

1. Introduction

The foreign body response (FBR) to implantable devices is a physiological reaction that occurs when an exogenous material is introduced into the body. Initially, the implantation of a foreign body triggers protein adsorption on the surface of the implant, attracting immune cells like neutrophils, monocytes, and macrophages [1,2]. The acute inflammatory phase, which normally lasts for the first 3 weeks, extends to chronic inflammation in the presence of an implant [3,4]. This phase is marked by prolonged macrophage activity, shifting from proinflammatory (M1) to anti-inflammatory (M2) phenotypes [5–7]. However, at times this transition is delayed, leading to continued inflammation and formation of foreign body giant cells (FBGCs) [8]. Additionally, activated fibroblasts differentiate into myofibroblasts, secreting collagen and forming a fibrotic tissue that encapsulates the foreign material [9–11]. The extent of fibrosis can differ substantially

* Corresponding author. Department of Nanomedicine, Houston Methodist Research Institute, 6670 Bertner Avenue, R8-111, Houston, TX, 77030, USA.
E-mail address: agrattoni@houstonmethodist.org (A. Grattoni).

https://doi.org/10.1016/j.biomaterials.2025.123110
Received 2 May 2024; Received in revised form 5 December 2024; Accepted 12 January 2025
Available online 13 January 2025

based on the properties of the material used in the device.

Notably, chronic inflammation associated with FBR leads to enhanced secretion of angiogenic factors by activated macrophages and myofibroblasts potentially enhancing angiogenesis locally [7,12,13]. In the context of long-acting implantable drug delivery systems and injectable depots, fibrosis, and local collagen and vascularization density could affect the transport of drugs and their pharmacokinetics [14]. For instance, the presence of a dense fibrotic network surrounding a long-acting injectable depot was reported to hinder the dissolution and absorption of paliperidone palmitate, thereby affecting its plasma concentration [15]. Similarly, Whyte et al. reported impaired insulin release from an implantable delivery system due to fibrotic encapsulation [16].

Additionally, chronic exposure to locally-released therapeutics can exacerbate inflammation. For instance, Su et al. investigated the extended subcutaneous release of tenofovir alafenamide (TAF) via a semipermeable polyurethane reservoir in rabbits and non-human primates [17]. Over a 12-week period post-implantation, the TAF implants induced significant inflammation, fibrosis and necrosis at the implant site, affecting drug delivery.

In our previous work, we developed different drug delivery implants that employ a nanofluidic membrane to modulate the release of medications [18,19]. In one of these studies, we compared drug delivery implants made of 6Al4V titanium and polyether ether ketone (PEEK) which exhibited distinct FBR in non-human primates (NHP) [20]. Despite this, the sustained release of 2-hydroxypropyl-β-cyclo-dextrin-enhanced cabotegravir (βCAB) was comparable between the two types of implants. In a recent study, we investigated the local FBR to a titanium drug delivery implant for the administration of TAF in NHP [21]. We observed that the intensity of FBR was closely correlated with local concentration of TAF. However, this did not impact the biodistribution of the drug. Similarly, in a 20-month islatravir PK study in NHP using an ultra-long-acting subdermal implant, no inflection in plasma drug concentration was observed, indicating negligible effect of FBR on drug release long-term [19].

These contrasting findings prompted us to systematically investigate the effect of the FBR on drug delivery from implantable devices [22] composed of different biocompatible materials. It can be hypothesized that the transport and biodistribution of drugs could be affected by: 1) thickness and density of the fibrotic capsule, 2) vascularization of the tissue surrounding the implant and 3) size and physicochemical properties of the therapeutic molecule. Extensive research elucidated that for non-leaching biomaterials, fibrotic tissue is affected by material properties such as microtopography [23,24], wettability [25,26] and charge [27,28]. Therefore, in this study, we used implants made of biocompatible acrylic resin, nylon and polylactic acid (PLA) with distinct surface properties to elicit variable extents of foreign body response. First, we characterized the surface properties of the implants. Next, we assessed fibrotic capsule thickness, collagen composition, vascularization and lymphocytes infiltration induced by the implants at 2-, 6-, and 12-weeks post-implantation in rats. The fibrotic capsule collected at endpoint, was used to evaluate the diffusion of a small (293 Da) and a large (150 kDa) clinically relevant molecule (islatravir and IgG) through the fibrotic tissue to assess how molecule size affects transport properties. Finally, we performed a 12-week islatravir and IgG PK study in rats using subdermal long-acting drug delivery implants matching in size, shape and material properties as the previous experiment. As there is broad characterization of the FBR elicited by subcutaneously delivered drugs in the literature [21,29–31], here we focused on the effect of the FBR on drug delivery.

Ultimately, the study sought to provide a direct systematic and quantitative assessment of the effect of FBR on drug transport across fibrotic tissues. By eliminating variables such as implant size, shape, and properties, implantation site and duration, and animal models, the study offers a standardized strategy that could be adopted for other therapeutic molecules.

2. Materials and methods

2.1. Solid implants fabrication

Solid discoidal implantable devices were designed in Solidworks (Dassault System) with diameter of 15 mm and thickness of 3 mm. The implants were 3D printed with 3 different materials: acrylic resin (Biomed, Formlabs), nylon (PA2200, EOS) and polylactic acid (PLA, Makerbot). The acrylic resin devices were fabricated via stereolithography (Formlabs Form 3B), the nylon implants via selective laser sintering (Sculpteo) while the PLA ones were produced through fused deposition modeling (Lulzbot Mini 2). Prior to implantation, the devices were washed with 1 % Alconox detergent, rinsed in deionized water and sterilized via autoclave.

2.2. Degradation in accelerated conditions

Autoclaved implants (n = 4 per material) were dried for 1h at 60 °C followed by 1h in a vacuum chamber with silica beads and weighed to obtain the baseline weight. Then, the implants were placed in glass scintillation vials filled with 20 ml of simulated body fluid (SBF) and incubated in accelerated conditions at 67 °C for 10 days. Three times a week, the pH of the solution was measured and the samples were removed from the vials, dried as above, weighed and placed back in the vials. According to Arrhenius equation, we estimated that 10 days of incubation in accelerated condition at 67° correspond to approximately 80 days of incubation at 37°C [32].

2.3. Contact angle measurements

The surface of the discoidal implants was uniformly sanded using ultra fine 2000-grit sandpaper. The water contact angle of the sanded discoidal samples (n = 5/material) was measured using the Attension Theta system (Biolin Scientific) for imaging and the One Attension software (Biolin Scientific) for analysis.

2.4. Surface roughness assessment

Surface topography images of solid discoidal implants (n = 3/material) were acquired using a Keyence VK-X3000 profilometer. The acquired images were analyzed using the software Keyence VK-X3000 MultiFileAnalyzer 3.3.1 to calculate arithmetic mean height, maximum height of the profile and mean width of the profile element.

2.5. Scanning electron microscopy (SEM)

Solid discoidal implants were imaged with the Nova NanoSEM 230 at the Houston Methodist Research Institute (HMRI) SEM core. The samples were sputtered with 7 nm iridium and imaged using a 5 kV electron beam under high vacuum (10^{-3} Pa).

2.6. Animal experiments

Weight matched (250 g) male Sprague Dawley rats (Charles River, Houston, TX, USA) were used in this study. All animals were maintained and employed in conformity with guidelines established by the American Association for Laboratory Animal Science. Rats were kept in the HMRI animal facility and studies were conducted at the HMRI Comparative Medicine Program (CMP) according to provisions of the Animal Welfare Act, PHS Animal Welfare Policy, and the principles of the NIH Guide for the Care and Use of Laboratory Animals. The humane use of animals in research and all procedures detailed in the IACUC protocol number IS00007358 were approved by the Institutional Animal Care and Use Committee at HMRI. Animals were housed under standard conditions and had ad libitum access to water and a standard laboratory diet.

2.7. In vivo assessment of foreign body response

Solid discoidal implants were implanted in rats (n = 18) under anesthesia with 2 % isoflurane. Two 1 cm incisions were made on the back of the animal parallel to the spine. From each incision, two subcutaneous pockets were created by means of dissection on the flank of the animal, in order to accommodate one implant each (n = 4 implants/rat). The implants were placed on the animal flanks, between the panniculus carnosum, the characteristic skin muscle layer of rodent, and the oblique muscle. A subcuticular suture was performed to close the incision. Each animal was implanted with at least one implant of each material. The animals were divided in 3 groups, which were euthanized at different timepoints: 2, 6 and 12 weeks post-implantation. At each endpoint, the implants were explanted together with the surrounding tissue which was separated and used for histological assessments, FRAP and the diffusivity experiment.

2.8. Histology and immunohistochemistry analysis

After explant, the tissues were fixed in 10 % buffered formalin followed by dehydration in standard ethanol. Dehydrated tissues were washed in xylene and embedded in paraffin prior to sectioning (5 μm) at the HMRI pathology core, which performed the Hematoxylin-eosin (H&E) and Masson's Trichrome (MT) staining. Section scans and magnified fields of view (FOV) were acquired using the Keyence BZ-X810 automated microscope. Fibrotic capsule thickness measurements were performed on MT scans (n = 12 measurements per sample, n = 3–4 samples per group). Collagen fractional area analysis was performed via color deconvolution on n = 5–8 FOV per MT-stained section (n = 3–4 samples per group) using a custom script on QuPath. The fibrotic capsule area used for quantification in each FOV was segmented manually.

Immunofluorescence staining was performed on 5 μm sections. These were subjected to heat-induced epitope retrieval in rodent decloaker buffer (Biocare Medical) at 121 °C for 20 min followed by blocking in 5 % normal goat serum for 1 h at room temperature. Primary antibodies were incubated for 16 h at 4 °C in renaissance antibody diluent (Biocare Medical) and secondary antibodies for 1 h at room temperature in blocking buffer. Prolong Diamond mounting media with DAPI was added to preserve fluorescence (Invitrogen). Slides were visualized using the Keyence BZ-X810 automated microscope. Quantification of $CD45^+$ cells was obtained via semiautomated colocalization analysis performed in QuPath on 5 FOV per slide (n = 3–5 samples per group). $CD31^+$ blood vessels were manually quantified in QuPath on 5 FOV per slide (n = 3–5 samples per group). The fibrotic capsule area used for quantification in each FOV was segmented manually.

Antibodies used were: anti-CD45 (ab10558, Abcam, 2 μg/ml), anti-CD31/PECAM-1 (NB100-2284, Novus Bio, 0.5 μg/ml), AlexaFluor 555 goat anti-rabbit (A21428, Invitrogen, 4 μg/ml).

2.9. Collagen area, maturity and orientation assessment

Picrosirius red (PSR) staining was performed on sections from paraffin embedded fibrotic capsule tissue (Picrosirius red stain kit, Polysciences, 24901). The stained sections were acquired at 40× magnification with an Olympus FV3000 microscope equipped with an Olympus DP80 color camera (n = 5 FOV per sample, n = 3–4 samples per material and timepoint). Polarized light microscopy images were acquired in the same FOV using a linear polarizer and analyzer at a 0° and 45° angles with respect to the brightfield image with the use of a rotating stage.

Picrosirius red image analysis was performed with a semi-automated custom Matlab (2024a, Matworks) script using the plugin MIJ [33] according to previously published methods [34–37]. Polarized light images were manually registered and the maximum intensity projection (MIP) was obtained. Next the contour of the fibrotic capsule was manually outlined in the brightfield image and used as a mask for the MIP. Collagen fibers orientation was calculated from the MIP using the OrientationJ plugin [38,39] written by Daniel Sage at the Biomedical Image Group, EPFL, Switzerland (https://bigwww.epfl.ch/demo/orientation/). Then, the masked MIP was transformed from the RGB to the CIELAB color space. The contrast of the L* channel was automatically adjusted in ImageJ and the Huang threshold was applied to measure the collagen fractional area. The green component of the image, which corresponds to type III collagen was extracted by selecting only the pixel with negative values in the a axis channel.

2.10. Fluorescence recovery after photobleaching (FRAP)

Freshly explanted tissues were incubated overnight at 4 °C with a 2 mg/ml solution of either FITC (Invitrogen) or IgG-FITC (Sigma) in tissue culture media (DMEM/F12, Gibco). After incubation, the tissues were removed from the media solutions and placed in microscope chamber slides (Nunc Lab-Tek II, Thermofisher). The tissue diffusion coefficients were assessed as previously described [40,41].

2.11. Diffusivity experiment

A custom-made diffusion chamber, inspired by the setup presented by Wood et al. [42] was designed in Solidworks and 3D printed in biocompatible photocurable resin (Biomed, Formlabs) via stereolithography (Formlabs Form 3B). The chamber is made of two compartments of different sizes, the smallest with a capacity of 0.25 ml is designed as the drug reservoir, while the largest contains 1.5 ml of sink solution. The fibrotic capsule that formed around the implants is dissected and immediately secured between the two reservoirs and locked in place with a clamping mechanism (Fig. 4E). Then the sink reservoir was loaded with 1.5 ml of tissue culture media (DMEM/F12, Gibco) while 0.25 ml of a solution with 1 mg/ml of islatravir and IgG-FITC was loaded in the drug reservoir. The larger compartment was sealed with parafilm while the other was closed with a silicone plug. The assembled chamber was incubated at 37 °C for 5 days, and every 24 h, the sink solution was collected for drug quantification and replaced with fresh media.

Drug quantification was performed via high-performance liquid chromatography (HPLC) as previously described for the islatravir [19,43], and via fluorescence measurement in a plate reader (Synergy H4, Biotek) for the IgG-FITC.

According to Fick's law of diffusion:

$$\frac{\Delta m}{\Delta t^* A_{FC}} = P_{FC}{}^* \Delta C$$

where Δm is the difference between the molecule mass loaded in the drug reservoir and the molecule mass measured at every timepoint, Δt is the time between sample collections, A_{FC} is the exchange surface area of the fibrotic tissue, P_{FC} is the fibrotic capsule permeability and ΔC is the difference in concentration between the drug reservoir and the sink reservoir. The fibrotic capsule permeability is derived as follows:

$$P_{FC} = \frac{\Delta m}{\Delta C^* \Delta t^* A_{FC}}$$

From the permeability, the diffusion coefficient is obtained as follows:

$$D_{FC} = P_{FC}{}^* d_{FC}$$

where d_{FC} is the thickness of the fibrotic capsule clamped in the diffusion chamber.

2.12. Drug delivery implants fabrication

The reservoir-based discoidal implants were designed to have the same dimensions of the solid ones and were fabricated with the same

materials and 3D printing techniques. The implants were made by a hollow discoidal drug reservoir and a lid having a slot to house a nanofluidic silicon membrane fabricated according to a previously described protocol [44]. All the components were washed in 1 % Alconox, rinsed in deionized water, sterilized via autoclave (polymeric parts) or 100 % isopropyl alcohol (silicone membranes) and assembled and loaded under a laminar flow hood in sterile conditions. The membrane was attached to the lid using biocompatible UV epoxy (MED-OG116-31, Epotek). The PLA drug reservoir was coated with a thin layer of biocompatible thermal epoxy (MED-302-3 M, Epotek) to prevent leakage. About 30 mg of Islatravir (MK-8591, MedChemExpress) or human IgG (Innovative Research) were loaded in powder form in the discoidal reservoir and packed using a syringe plunger. The implants were weighed before and after loading to measure the exact amount of drug loaded in each device. The lid-membrane assembly was placed on the reservoir and sealed using UV epoxy.

2.13. In vitro release experiment

The reservoir-based implants loaded with islatravir and IgG were placed in 50 ml centrifuge tubes with 5 ml of PBS +0.02 % sodium azide. The tubes were incubated at 37 °C on an orbital shaker under constant

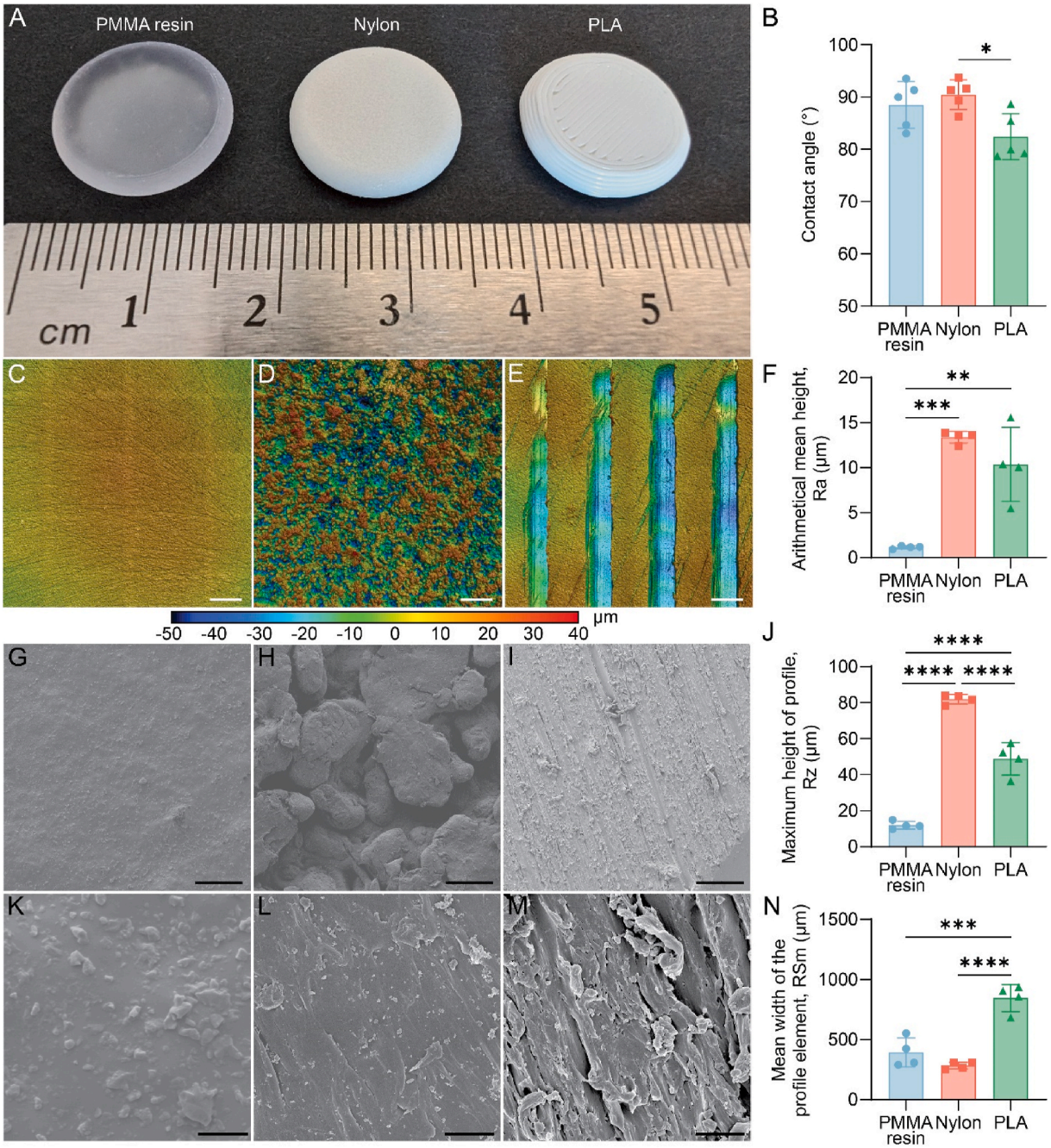

Fig. 1. Implants characterization. A) Optical image of the 3D printed implants. B) Contact angle measurements. Surface profilometry scans of C) PMMA resin, D) nylon, and E) PLA implants. Scale bar 400 μm. F) Arithmetical mean height of the peaks detected on the surface of the material via surface profilometry. SEM images at 1000× magnification of G) PMMA resin, H) nylon and I) PLA implants. Scale bar 50 μm. J) Maximum height of the profile detected on the surface of the material via surface profilometry. SEM images at 10000× magnification of K) PMMA resin L) nylon and M) PLA implants. Scale bar 5 μm. N) Mean width of the profile element detected on the surface of the material via surface profilometry. One-way ANOVA, *$p < 0.05$, **$p < 0.01$, ***$p < 0.001$, ****$p < 0.0001$.

agitation. The sink solution was collected and replaced every other day. islatravir and IgG content was measured via HPLC and microBCA (Invitrogen) respectively.

2.14. In vivo pharmacokinetic study

Sprague Dawley rats (n = 24) are divided in 3 groups: resin, nylon and PLA which received implants of the respective materials. Each animal was implanted subcutaneously with a device loaded with islatravir and with one containing IgG contralaterally. Blood collection was performed at day 3, 7, 14, 28, 42, 56 and 84 post-implantation using K_2EDTA microtainer tubes (BD). Blood samples are centrifuged at 10000 g for 12 min to separate the plasma which is collected and stored at −80 °C. Plasma concentration of islatravir was quantified via liquid chromatography/mass spectroscopy, while IgG was quantified with a human IgG ELISA kit (Abcam).

At endpoint, the implants were removed and stored at −80 °C while the tissue surrounding the implants was retrieved and processed for histological analysis as described above.

For residual quantification, islatravir and IgG implants were thawed, drilled, placed in 5 ml of dimethyl sulfoxide (DMSO) and PBS + 0.02 % sodium azide respectively and flushed using a syringe with an 18G needle and the implant's own solution. The implants were left on an orbital shaker at 4 °C overnight to allow complete dissolution of the drugs. The solutions of islatravir and IgG were then filtered using 0.2 μm centrifugal filter and quantified via HPLC and ELISA respectively.

2.15. Statistical analysis

Data are represented as average ± standard deviation unless otherwise noted. Tukey's Honest Significance test is used as a post-hoc test for multiple comparison after one-way and two-way ANOVA. Statistical analysis was performed with Graphpad Prism 10.4.

3. Results

3.1. Implants fabrication and characterization

The discoidal implants were fabricated with different 3D printing techniques using biocompatible, non-biodegradable (Fig. S1) materials, to achieve distinct surface features. Macroscopically, the PMMA resin and nylon implants have a smoother texture, while individual 3D printed layers and extruded strands are clearly noticeable on the PLA implant (Fig. 1A). To avoid the confounding effect of the surface features, wettability was assessed on uniformly smoothened surfaces. PMMA resin and nylon implants showed similar contact angles while PLA was more hydrophilic (Fig. 1B). This minimal, although significant increase in wettability is still not sufficient to have a meaningful effect in limiting protein adsorption at the early stage of FBR [45]. 3D surface topography scans obtained via optical profilometry revealed profound differences across the materials. The resin implants exhibit a smooth surface (Fig. 1C), typical of SLA 3D printing, where photopolymer liquid resin is selectively cured to form a solid object. Differently, SLS technology, which uses lasers to bind finely powdered materials together into a solid structure, generates a grainy surface on the nylon discs (Fig. 1D). The PLA implants had the least uniform topography, with a smooth surface in correspondence to the extruded strands of material alternated by dips between the strands (Fig. 1E), a common feature of FDM 3D printed parts [46]. Accordingly, profilometry analysis showed that nylon and PLA discs had an overall rougher surface compared to the resin implants (Fig. 1F–J) which was confirmed by low magnification SEM images (Fig. 1G–I). As expected, the mean width of the profile element on PLA implants was significantly higher compared to the other implants (Fig. 1N). At the microscopic level, the surface of resin and nylon appeared similar, whereas the PLA had a less uniform texture (Fig. 1K–M).

3.2. Assessment of the foreign body response to discoidal implants

The 3 types of discoidal devices were subcutaneously implanted on the flanks of Sprague Dawley rats, between the panniculus carnosum and the oblique muscle of 3 groups of rats. At 2-, 6- and 12-weeks post-implantation, a group of animals was euthanized and the fibrotic capsule and subcutaneous tissue surrounding the implants was collected for histological and ex-vivo diffusivity analyses. Across the 3 types of materials, tissue sections stained with H&E showed an overall mild FBR with no sign of significant immune cell infiltration and giant cell formation (Fig. 2A). MT-stained tissue sections revealed a collagen-rich, fibrotic capsule (Fig. 2B), thicker around PLA implants compared to the resin and nylon ones at weeks 2 and 6 post-implantation (Fig. 2C). By week 12, the fibrotic capsule surrounding resin and nylon implants reached a thickness similar to the PLA discs (Fig. 2C). The fibrotic capsule thickness of the PLA remained constant over the 12-week implantation duration, whereas the nylon implants gradually increased. Regional quantification of the fibrotic capsule thickness around the implants revealed a consistently thinner capsule near the curved edges of the implants compared to the flat edges (Fig. S2). Despite the change in fibrotic capsule thickness, only a slight but insignificant decrease in collagen density, assessed via color deconvolution on MT-stained sections, was observed across implant materials over time (Fig. 2D). Similar results were obtained by quantifying the collagen fractional area on polarized light microscopy images of picrosirius red-stained sections (Figs. S3A–D). Furthermore, the quantification of type III collagen via color deconvolution performed on the same images, revealed no significant differences in collagen maturity across timepoints (Fig. S3E). The collagen fibers appeared to be mostly aligned to the surface of the implants (Fig. 2E–G) or, less predominantly at a ~45° angle (Figs. S3F–H) with no significant differences across timepoints or implant materials.

Immunofluorescence staining of lymphocyte on fibrotic tissue sections was performed (Fig. 3A) to assess cell density and immune cell infiltration. We observed a decreasing trend in cell density over time across the 3 implant materials, consistent with a resolving FBR (Fig. 3B), while the ratio of CD45-positive vs DAPI-positive cells remained constant at all time points (Fig. 3C).Additionally, fibrotic capsule vascularization was evaluated on H&E and CD31-stained tissue sections (Fig. 3D–S4A, B). At all times, blood vessel density and relative area remained consistent for the 3 implant types (Fig. 3E and F), comparably to what has been measured in the skin [40].

Overall, resin and nylon implants appear to have elicited a milder response during the acute phase of the FBR compared to PLA. In general, all implants exhibited a biocompatible profile in terms of fibrotic capsule thickness and immune cell recruitment [47,48], eliciting a moderate response both in the acute and chronic phase of the FBR.

3.3. Ex-vivo assessment of drug transport through fibrotic tissue

The fibrotic tissue that forms around implants has the potential to act as a physical barrier to the delivery of drugs from implantable devices [14,15,47,49]. Therefore, we sought to evaluate the transport properties of the fibrotic capsule that formed around the discoidal implants using clinically relevant therapeutic molecules of different sizes, islatravir (293 Da) and IgG (150 kDa). The diffusion coefficient evaluation performed via FRAP (Fig. 4A) revealed an overall higher diffusivity of islatravir compared to IgG (Fig. 4B–D), attributable to its smaller size. Further, the fibrotic capsule of resin implants appears to be opposing the least resistance to islatravir diffusion. To further assess the transport properties of the fibrotic tissue that formed around the implants, we designed an ex-vivo diffusion chamber (Fig. 4E) where the fibrotic capsule is clamped between two reservoirs of different sizes immediately after explant. The smallest reservoir contained a concentrated drug solution, while the other, filled with tissue culture media acted as a sink. The difference in concentration between the two compartments drives

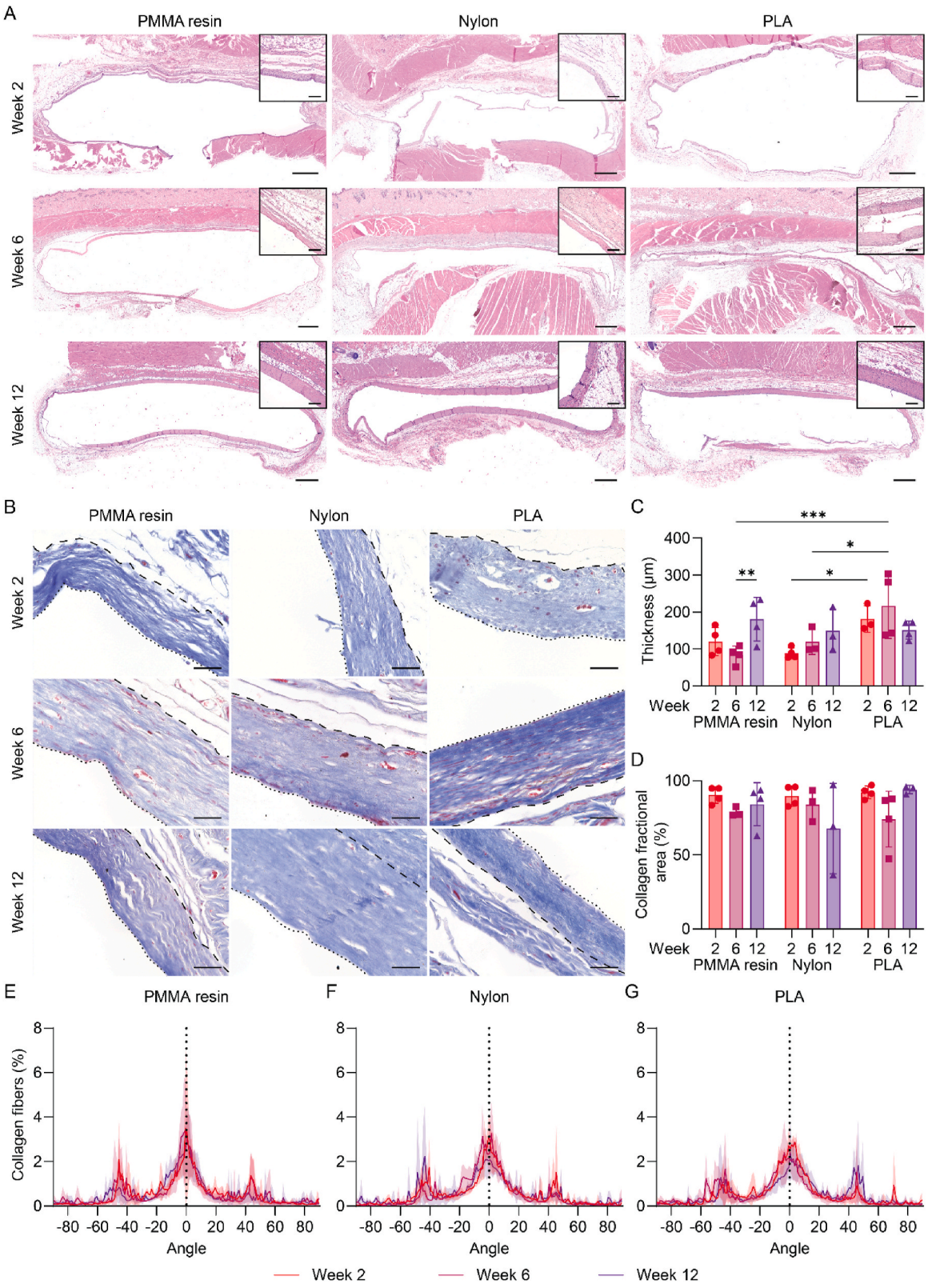

Fig. 2. Immunohistochemistry analyses of fibrotic capsule tissue. A) Scans of H&E stained slides of the subcutaneous tissue surrounding PMMA resin, nylon and PLA implants explanted at 2, 6 and 12 weeks post-implantation. Scale bar 1 mm. 40× magnifications in insets. Scale bar 50 μm B) Images of MT-stained slides of the fibrotic capsule surrounding PMMA resin, nylon and PLA implants explanted at 2, 6 and 12 weeks post-implantation. Dotted line represents the edge of the capsule in contact with the implant while dashed line represents the edge in contact with the subcutaneous tissue. Scale bar 50 μm. C) Fibrotic capsule thickness and D) collagen fractional area measured on MT slides. Distribution of collagen fibers orientations across timepoints in fibrotic capsules surrounding E) PMMA resin, F) nylon and G) PLA implants (n = 3–4/timepoint). Two-way ANOVA *$p < 0.05$, **$p < 0.01$, ***$p < 0.001$.

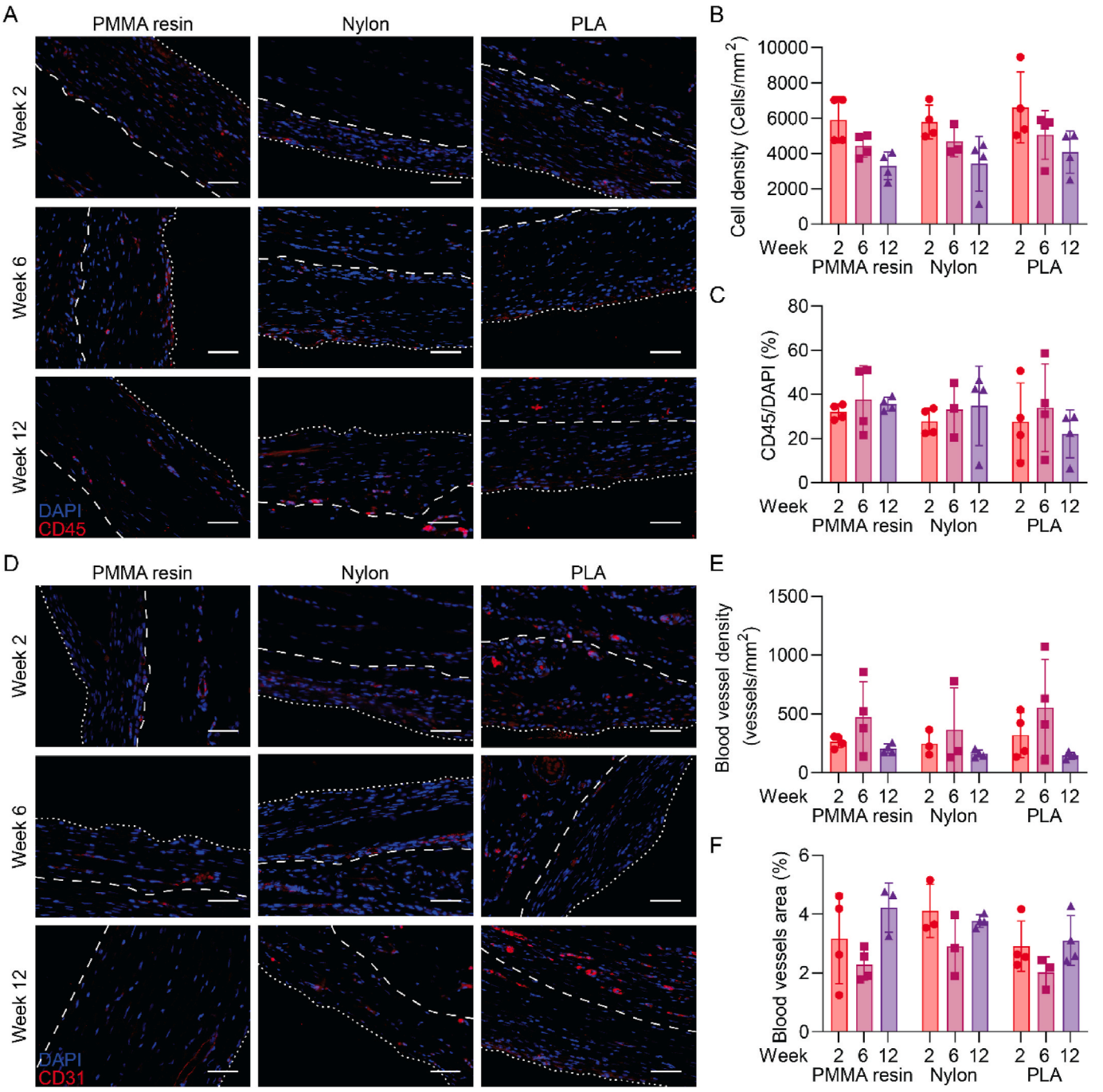

Fig. 3. Lymphocyte infiltration and vascularization of the fibrotic capsule. A) Images of CD45+DAPI-stained slides of the fibrotic capsule surrounding PMMA resin, nylon and PLA implants explanted at 2, 6 and 12 weeks post-implantation. Dotted line represents the edge of the capsule in contact with the implant while dashed line represents the edge in contact with the subcutaneous tissue. Scale bar 50 μm. B) Overall cell density and C) percentage of $CD45^{+}$ cells within fibrotic tissue. D) Images of CD31+DAPI-stained slides of the fibrotic capsule surrounding PMMA resin, nylon and PLA implants explanted at 2, 6 and 12 weeks post-implantation. Dotted line represents the edge of the capsule in contact with the implant while dashed line represents the edge in contact with the subcutaneous tissue. Scale bar 50 μm. E) Blood vessel density and F) fractional area measured on CD31-stained sections. Two-way ANOVA *$p < 0.05$.

the diffusion of the drug across the fibrotic capsule into the sink reservoir. Drug concentration measurements in the sink reservoir, collected over the course of 5 days, were used to calculate the cumulative amount of drug that diffused across the fibrotic tissue. As expected, islatravir exhibited faster diffusion kinetics compared to IgG (Fig. 4F) with no significant differences across timepoints (Fig. S5). These data was then used to calculate the permeability of the fibrotic capsule according to Fick's law of diffusion. Interestingly, the permeability exhibited a slight increasing trend over the timepoints, particularly for the fibrotic tissue that surrounded resin devices (Fig. 4G and H). The thickness of the fibrotic capsule employed in the diffusion chamber was measured histologically and used to calculate the diffusivity of the molecules. This analysis confirmed the increasing trend observed with the permeability assessment, especially for what concerns the islatravir, suggesting that the thickness of the fibrotic capsule might not play a significant role in limiting drug diffusion (Fig. 4I and J).

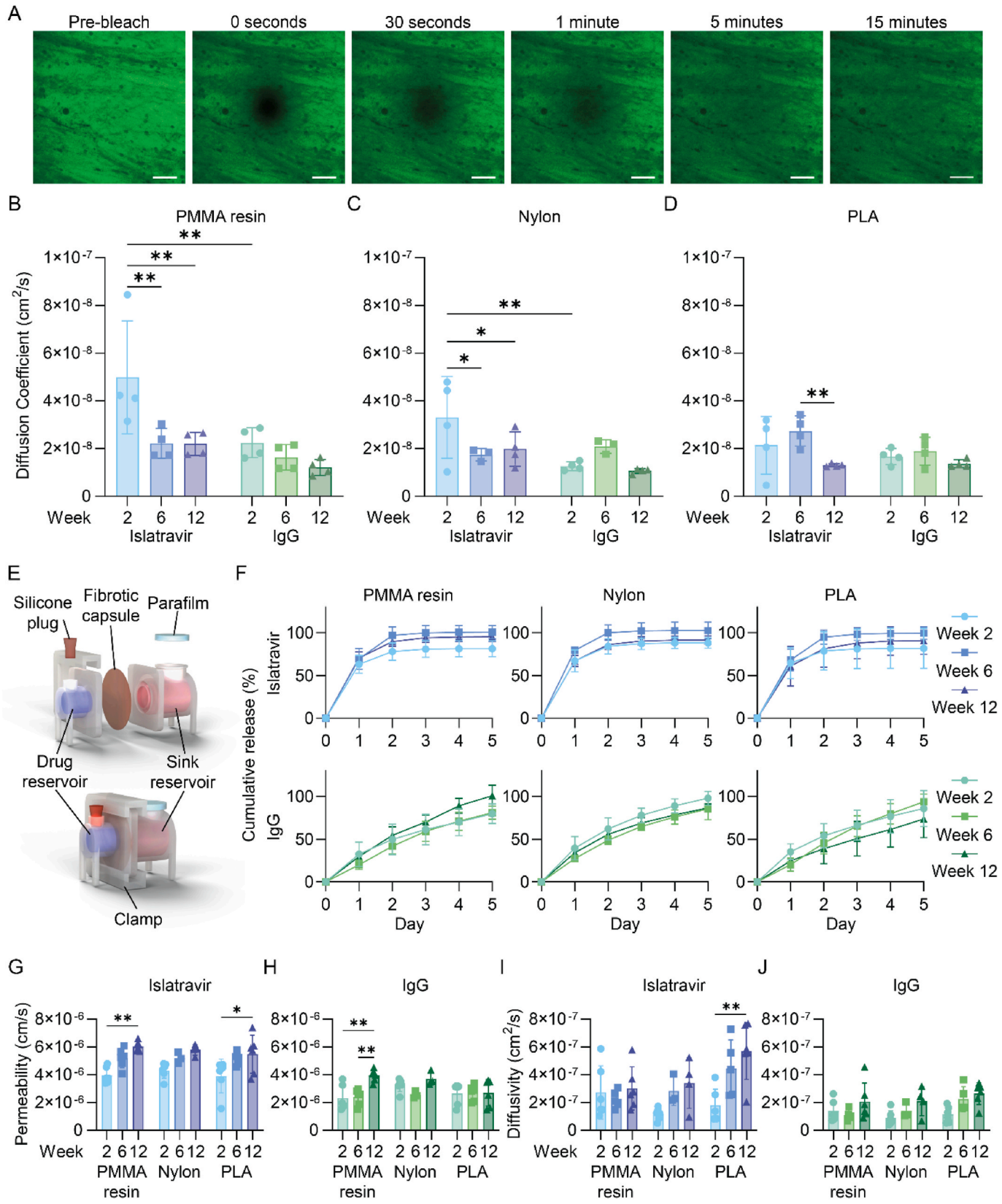

Fig. 4. Islatravir and IgG transport through fibrotic tissue ex-vivo. A) Representative images of fibrotic tissue acquired during FRAP experiment. Scale bar 100 μm. Diffusion coefficient of islatravir and IgG in fibrotic tissue calculated from FRAP analysis for B) PMMA resin, C) nylon and D) PLA implants. E) Schematic of the ex-vivo diffusion chamber. F) Cumulative release of islatravir and IgG through the fibrotic capsule clamped in the diffusion chamber (n = 4–6/timepoint). Permeability of G) islatravir and H) IgG through fibrotic tissue calculated from cumulative release data. Diffusivity of I) islatravir and J) IgG through fibrotic tissue calculated from cumulative release data. Two-way ANOVA *$p < 0.05$, **$p < 0.01$.

3.4. Effect of fibrotic encapsulation on pharmacokinetic of drugs

The ex-vivo assessments pointed at minimal differences in terms of drug transport across the fibrotic capsule generated by different materials. More significant variations were observed across timepoint, where the diffusivity of drugs increased over time. To further investigate these aspects, we designed an implantable reservoir-based drug delivery device with the same outer shape, size and materials of the solid discoidal implants (Fig. 5A). The reservoir implant was made of a hollow reservoir, loaded with powder islatravir or IgG, and a lid attached to the reservoir with a minimal amount of biocompatible epoxy. The lid housed a nanofluidic membrane developed in our laboratory and used to control and extend the release of drugs [19,44]. After drug loading, the devices were subcutaneously implanted in rats. The drug kinetics in plasma were monitored with periodical blood draws and subsequent drug quantification over 3 months (Fig. 5B). The plasma concentration of islatravir remained constant throughout the study with an average of 1.85 ng/ml (Fig. 5C). Differently, IgG plasma levels exhibited a biphasic behavior, with an average of 9.30 μg/ml in the first 14 days followed by a ~200-fold decrease down to 35.95 ng/ml from day 28 to the end of the study (Fig. 5D and E). Similar trends were observed in vitro, where the islatravir released an average of 71.39 μg/day in a steady sustained fashion, while the IgG shows an initial burst release followed by a steady phase where the implants released 213.11 μg/day in average (Fig. 5F). To compare the in vitro release profile with the delivery kinetics in vivo, we measured the residual drug in the implant after explant. We observed that the implants loaded with islatravir released ~20 % of their content while the ones loaded with IgG released 80–90 % of the total (Fig. 5G and H). These measurements translate into an estimated daily release of 74.77 μg/day for islatravir and 281.68 μg/day for the IgG on average (Fig. 5I and J).

Finally, we performed a histological assessment of the tissue surrounding the implants at endpoint via H&E, MT, DAPI-CD45 and DAPI-CD31 staining (Fig. 6A, B, E, H). Thickness and collagen density analysis

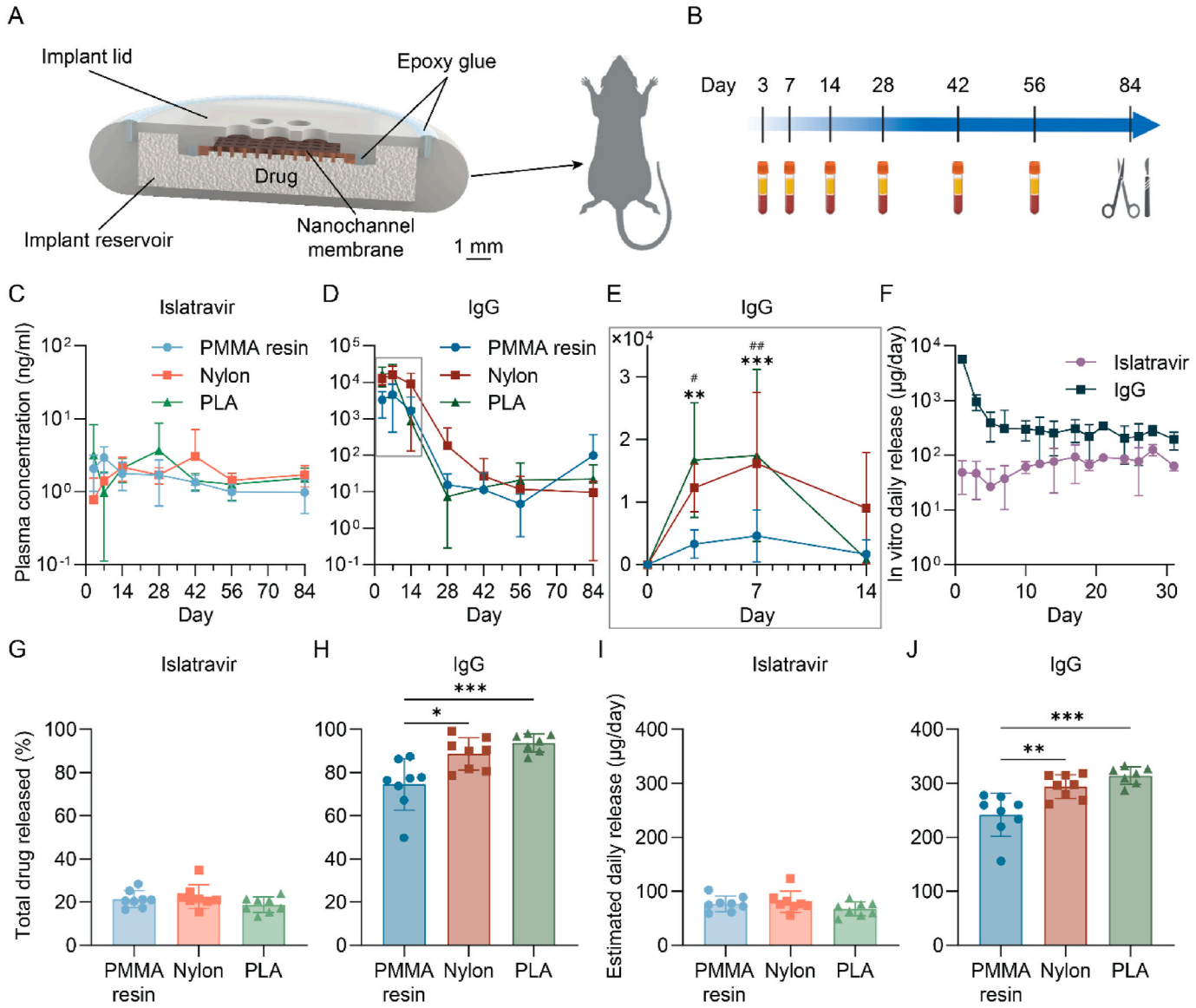

Fig. 5. PK study. A) Schematics of implantable reservoir-based drug delivery device. B) Experimental timeline. Plasma pharmacokinetic of C) islatravir and D) IgG released from reservoir devices made of PMMA resin, nylon and PLA (n = 6–8/timepoint). Gray box indicates the portion of the plot magnified in panel E. E) Initial release of IgG from reservoir devices made of PMMA resin, nylon and PLA (n = 6–8/timepoint). (# Nylon vs PMMA resin, * PLA vs PMMA resin) F) In vitro daily release of islatravir and IgG from reservoir devices (n = 4/molecule). Total G) islatravir and H) IgG released from reservoir devices during the PK study calculated from residual drug measurement. Estimated daily release of I) islatravir and J) IgG based on residual drug measurements. One-way ANOVA # *p < 0.05, ## **p < 0.01, ***p < 0.001.

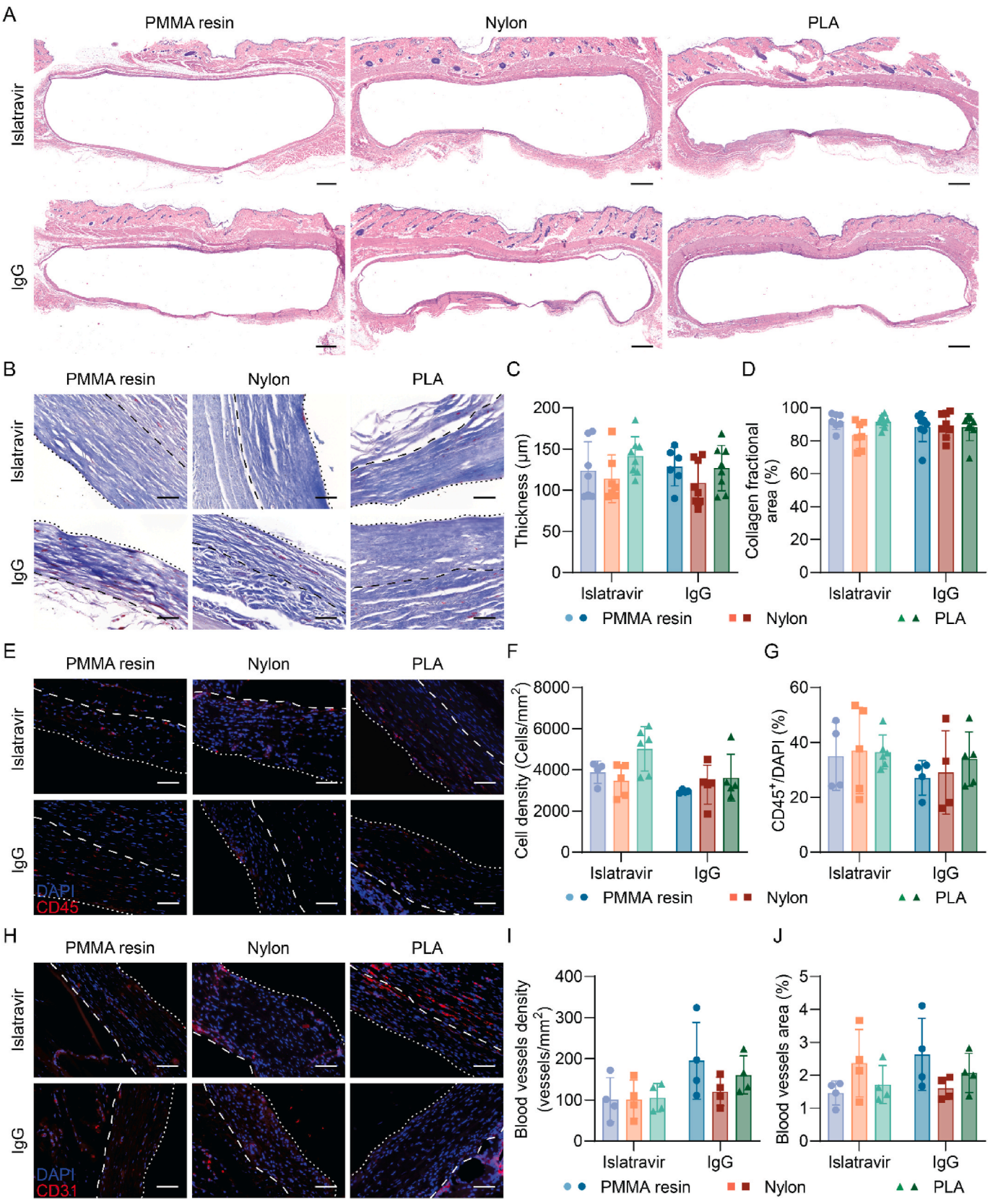

(caption on next page)

Fig. 6. Histological analyses of fibrotic capsule tissue from PK experiment. A) Scans of H&E-stained slides of the subcutaneous tissue surrounding PMMA resin, nylon and PLA implants loaded with islatravir and IgG explanted at 12 weeks post-implantation. Scale bar 1 mm. B) Images of MT-stained slides of the fibrotic capsule surrounding PMMA resin, nylon and PLA implants loaded with islatravir and IgG explanted at 12 weeks post-implantation. Dotted line represents the edge of the capsule in contact with the implant while dashed line represents the edge in contact with the subcutaneous tissue. Scale bar 50 μm. C) Fibrotic capsule thickness and D) collagen fractional area measured on MT slides. E) Images of CD45+DAPI-stained slides of the fibrotic capsule surrounding PMMA resin, nylon and PLA implants loaded with islatravir and IgG explanted at 12 weeks post-implantation. Dotted line represents the edge of the capsule in contact with the implant while dashed line represents the edge in contact with the subcutaneous tissue. Scale bar 50 μm. F) Overall cell density and G) percentage of $CD45^+$ cells within fibrotic tissue. H) Images of CD31+DAPI-stained slides of the fibrotic capsule surrounding PMMA resin, nylon and PLA implants loaded with islatravir and IgG explanted at 12 weeks post-implantation. Dotted line represents the edge of the capsule in contact with the implant while dashed line represents the edge in contact with the subcutaneous tissue. Scale bar 50 μm. I) Blood vessel density and J) fractional area measured on CD31-stained slides. Two-way ANOVA.

showed no significant differences across groups (Fig. 6C and D), consistently to what was observed for the chronic phase of the FBR in the previous study (Fig. 2C–D). Importantly, the localized delivery of islatravir and IgG appears to not exacerbate the FBR in the subcutaneous tissue (Fig. 6E–G, Fig. 3A–C). Similarly, the vascularization was not affected by the local release of drugs (Fig. 6H–J, Fig. 3D–F)

4. Discussion

In this study, we performed an extensive characterization of the foreign body response to biocompatible implantable devices and its impact on molecule diffusion and drug delivery.

Firstly, we designed and employed solid implants made of PMMA resin, nylon and PLA with different surface properties to trigger distinct extents of FBR. All the materials exhibited stability for up to the equivalent of 80 days at body temperature in an in-vitro degradation study in accelerated condition. Furthermore, the devices did not alter the pH of the SBF sink solution over the course of the experiment, making them good candidates for the in-vivo study (Fig. S1).

For the FBR assessment, the devices were implanted in a subcutaneous pocket on the flank of the rats. The subcutaneous site, particularly in the inner arm or abdomen, is often chosen for the clinical deployment of polymeric implants for drug delivery or cell encapsulation as it allows for facile implantation, transcutaneous manipulation and retrieval [14,50]. Two weeks post-implantation, we observed differences in fibrotic capsule thickness which evened when the FBR was in its chronic stage. In particular, it appeared that PLA discs elicited a stronger FBR during the acute phase (Fig. 2A–C). The overall roughness of PLA implants was comparable to the PMMA resin implants. However, the filament deposition pattern on the surface of the PLA implants resulted in larger features with a sharper profile captured by the RSm (Fig. 1C–N) which could have contributed to a thicker fibrotic capsule during the acute phase of the FBR. Generally, features in the microscale and larger than the diameter of immune cells can exacerbate the FBR and a similar effect can be observed in implants presenting sharp angles [24,47,51–54].

Interestingly, the fibrotic capsule thickness was not uniform along the surface of the implant. The capsule was thinner at the interface with the curved section and thicker where it was in contact with flat surfaces (Fig. S2). These observations are in agreement with a study from Li et al. where the authors measured thicker fibrotic capsule along the flat portion of hydroxyapatite disks implanted subcutaneously in rats [55].

Collagen density characterization was performed via color deconvolution on MT-stained section of fibrotic tissue, showing consistent collagen composition of the capsule over time and across materials (Fig. 2B–D). Despite the existence of more advanced techniques for collagen quantification, such as second harmonic generation, these require specialized equipment that is not always readily accessible. Therefore, we validated our collagen assessment via polarized light microscopy imaging of picrosirius stained slides, obtaining results comparable to color deconvolution (Figs. S3A–D). Furthermore, this technique allowed us to assess collagen maturity, by quantifying type III collagen density (Fig. S3E), and collagen fibers orientation (Fig. 2E–G, Figs. S3F–H). As expected, the collagen fibers were predominantly aligned with the interface of the implant, while there were no significant differences in orientation and collagen maturity across timepoints and materials. Overall, our results suggest that within 2–12 weeks post-implantation, changes in collagen composition in the fibrotic capsule are limited.

Further histological analyses revealed a decrease in cellularity over time with a stable relative presence of $CD45^+$ cells and vascularization (Fig. 3) suggesting a slowly-evolving chronic foreign body response to the implants. To this end, a future more extensive immunological characterization of the microenvironment could provide valuable insights on the FBR to these biomaterials.

However, this work focuses on how FBR affect the transport and delivery kinetics of drugs. Therefore, we sought to assess the transport properties of clinically relevant therapeutic molecules through the fibrotic tissue ex-vivo (Fig. 4). To this extent, a custom-made diffusion chamber was employed to evaluate permeability and diffusivity of islatravir and IgG through the capsule (Fig. 4E). The smaller islatravir generally exhibited higher transport parameters compared to IgG. Differently, diffusion coefficients estimates over the course of the FBR appear to have contrasting trends. However, it is worth noting that FRAP was performed with the fibrotic capsule placed flat against the microscope slide. Therefore, with FRAP we evaluated the diffusion coefficient of molecules that move along the direction of the collagen fibers. Instead, with the diffusion chamber, we examined the diffusion across the tissue. In fact, the collagen in the fibrotic tissue appears to be anisotropic [56,57], with a preferential orientation of the fibers parallel to the implant surface (Fig. 2E–G, Figs. S3F–H). This hints to an increased resistance to the diffusion of molecules across the fibrotic tissue, substantiated by the lower diffusivity values obtained with the diffusion chamber. Finally, the increasing diffusivity trend observed with the diffusion chamber matches with the slight decrease in cell density observed in the chronic phase of the FBR (Figs. 3B and. 2D).

For the second phase of our study, we designed an implantable reservoir-based drug delivery device, having the same size and materials as the solid implants to elucidate the effect of the FBR on drugs pharmacokinetic. The devices were loaded with islatravir and IgG and implanted in rats for 3 months (Fig. 5A–B). Our results showed no differences in the plasma concentrations of islatravir across the different implant materials (Fig. 5C). Contrarily, the IgG loaded PMMA resin devices exhibited a lower release rate compared to nylon and PLA implants in the first 14 days (Fig. 5D and E), consistent with the lower fibrotic capsule permeability observed in our ex vivo study (Fig. 4H). This is also reflected in the total drug released (Fig. 5H) and subsequent estimated daily release (Fig. 5J). Overall, IgG levels in plasma were significantly higher than islatravir, especially in the first 14 days. These discrepancies in release kinetic appear to be counterintuitive, as islatravir has a significantly smaller molecular weight than IgG. However, their solubilities differ greatly, with islatravir that can be dissolved in PBS at maximum 1.35 mg/ml while IgG solubility is at least 20-fold higher. We postulate that the solubility and solubilization kinetics of the drugs, which were incorporated into the implant in powdered form, are primary factors that together with the nanochannel size and number determine their release rate. This hypothesis is corroborated by the results of the ex-vivo release experiment, where both islatravir and IgG were loaded in solution at 1 mg/ml, below the solubility limit of islatravir. In this scenario, the solubilization kinetics of the drugs cannot

play a role in their release kinetic, and therefore we observe faster release of islatravir compared to IgG (Fig. 4F).

Finally, the histological evaluation of the fibrotic capsules surrounding the drug-delivery implants (Fig. 6) closely aligned with the findings from the fibrotic tissue analysis around solid implants after 12 weeks of implantation. We propose that these results, along with the consistency between in-vitro release kinetics and in-vivo plasma pharmacokinetics for both molecules, as well as the stable plasma levels of islatravir, suggest that variations in the foreign body response (FBR) caused by the drugs have minimal impact on drug delivery.

5. Conclusion

Our study demonstrates that the foreign body response (FBR) has minimal impact on the delivery of small molecules from biocompatible implants, as evidenced by consistent plasma concentrations of islatravir across different materials. However, the fibrotic encapsulation may influence the release rate of larger molecules, such as IgG, during the acute phase of the FBR. These findings underscore the importance of considering the effects of fibrotic tissue, particularly in the early stages, when designing implantable drug delivery systems for larger therapeutic agents.

CRediT authorship contribution statement

Simone Capuani: Writing – review & editing, Writing – original draft, Visualization, Validation, Methodology, Investigation, Formal analysis, Data curation, Conceptualization. **Nathanael Hernandez:** Methodology, Investigation, Data curation. **Jocelyn Nikita Campa-Carranza:** Data curation, Investigation, Methodology. **Nicola Di Trani:** Data curation, Investigation, Methodology. **Takuma Yoshikawa:** Methodology, Investigation, Formal analysis. **Marco Farina:** Investigation. **Ashley L. Joubert:** Investigation. **Camden A. Caffey:** Investigation. **Alessio Simeone:** Investigation. **Seo Won Cho:** Investigation. **Patrick S. Stayton:** Validation, Supervision, Project administration, Funding acquisition. **Corrine Ying Xuan Chua:** Writing – review & editing, Visualization. **Alessandro Grattoni:** Writing – review & editing, Validation, Supervision, Project administration, Funding acquisition, Conceptualization.

Funding

This work was supported by funding from the National Institutes of Health National Institute of Allergy and Infectious Diseases R01AI167659 (AG, PS) and R01AI165372 (AG), and from the National Cancer Institute R01CA257563 (PS). AG, SC, MF, and CYXC are inventors of intellectual property licensed by Continuity Biosciences.

Declaration of competing interest

The authors declare the following financial interests/personal relationships which may be considered as potential competing interests: Alessandro Grattoni reports financial support was provided by National Institute of Allergy and Infectious Diseases. Patrick S. Stayton reports financial support was provided by National Institute of Allergy and Infectious Diseases. Patrick S. Stayton reports financial support was provided by National Cancer Institute. Alessandro Grattoni has patent licensed to Continuity Biosciences. Simone Capuani has patent licensed to Continuity Biosciences. Marco Farina has patent licensed to Continuity Biosciences. Corrine Ying Xuan Chua has patent licensed to Continuity Biosciences. If there are other authors, they declare that they have no known competing financial interests or personal relationships that could have appeared to influence the work reported in this paper.

Acknowledgements

We thank Dr. Jianhua (James) Gu from the electron microscopy core of Houston Methodist Research Institute, Yuelan Ren and Sandra Steptoe from the research pathology core of Houston Methodist Research Institute and Dr. Stefano Serpelloni for advice on contact angle measurements and analysis.

Appendix A. Supplementary data

Supplementary data to this article can be found online at https://doi.org/10.1016/j.biomaterials.2025.123110.

Data availability

Data will be made available on request.

References

[1] T. Horbett, The role of adsorbed proteins in tissue response to biomaterials, Biomater. Sci.: an introduction to materials in medicine 2 (2004) 237–246.
[2] B.O.O. Boni, L. Lamboni, T. Souho, M. Gauthier, G. Yang, Immunomodulation and cellular response to biomaterials: the overriding role of neutrophils in healing, Mater. Horiz. 6 (2019) 1122–1137.
[3] J.M. Anderson, Inflammatory response to implants, ASAIO transactions 34 (1988) 101–107.
[4] O. Veiseh, A.J. Vegas, Domesticating the foreign body response: recent advances and applications, Adv. Drug Deliv. Rev. 144 (2019) 148–161, https://doi.org/10.1016/j.addr.2019.08.010.
[5] J. Kzhyshkowska, et al., Macrophage responses to implants: prospects for personalized medicine, J. Leukoc. Biol. 98 (2015) 953–962, https://doi.org/10.1189/jlb.5vmr0415-166r.
[6] J.A. Jones, et al., Proteomic analysis and quantification of cytokines and chemokines from biomaterial surface-adherent macrophages and foreign body giant cells, J. Biomed. Mater. Res. 83A (2007) 585–596, https://doi.org/10.1002/jbm.a.31221.
[7] J.M. Anderson, A. Rodriguez, D.T. Chang, Foreign body reaction to biomaterials, Semin. Immunol. 20 (2008) 86–100, https://doi.org/10.1016/j.smim.2007.11.004.
[8] C. Chu, et al., Modulation of foreign body reaction and macrophage phenotypes concerning microenvironment, J. Biomed. Mater. Res. 108 (2019) 127–135, https://doi.org/10.1002/jbm.a.36798.
[9] B. Hinz, G. Gabbiani, Cell-matrix and cell-cell contacts of myofibroblasts: role in connective tissue remodeling, Thrombosis and haemostasis 90 (2003) 993–1002.
[10] Z. Sheikh, P.J. Brooks, O. Barzilay, N. Fine, M. Glogauer, Macrophages, foreign body giant cells and their response to implantable biomaterials, Materials 8 (2015) 5671–5701, https://doi.org/10.3390/ma8095269.
[11] S.F. Badylak, Host Response to Biomaterials: the Impact of Host Response on Biomaterial Selection, Academic Press, 2015.
[12] C.E. Witherel, D. Abebayehu, T.H. Barker, K.L. Spiller, Macrophage and fibroblast interactions in biomaterial-mediated fibrosis, Adv. Healthcare Mater. 8 (2019) 1801451.
[13] P. Martin, S.J. Leibovich, Inflammatory cells during wound repair: the good, the bad and the ugly, Trends Cell Biol. 15 (2005) 599–607.
[14] M. Farina, J.F. Alexander, U. Thekkedath, M. Ferrari, A. Grattoni, Cell encapsulation: overcoming barriers in cell transplantation in diabetes and beyond, Adv. Drug Deliv. Rev. 139 (2019) 92–115, https://doi.org/10.1016/j.addr.2018.04.018.
[15] N. Darville, et al., Intramuscular administration of paliperidone palmitate extended-release injectable microsuspension induces a subclinical inflammatory reaction modulating the pharmacokinetics in rats, J. Pharmaceut. Sci. 103 (2014) 2072–2087.
[16] W. Whyte, et al., Dynamic actuation enhances transport and extends therapeutic lifespan in an implantable drug delivery platform, Nat. Commun. 13 (2022) 4496.
[17] J.T. Su, et al., A subcutaneous implant of tenofovir alafenamide fumarate causes local inflammation and tissue necrosis in rabbits and macaques, Antimicrob. Agents Chemother. 64 (2020) e01893, https://doi.org/10.1128/AAC.01893-19, 01819.
[18] F.P. Pons-Faudoa, et al., Viral load reduction in SHIV-positive nonhuman primates via long-acting subcutaneous tenofovir alafenamide fumarate release from a nanofluidic implant, Pharmaceutics 12 (2020) 981.
[19] F.P. Pons-Faudoa, et al., Long-acting refillable nanofluidic implant confers protection against SHIV infection in nonhuman primates, Sci. Transl. Med. 15 (2023) eadg2887.
[20] F.P. Pons-Faudoa, et al., 2-Hydroxypropyl-β-cyclodextrin-enhanced pharmacokinetics of cabotegravir from a nanofluidic implant for HIV pre-exposure prophylaxis, J. Contr. Release 306 (2019) 89–96, https://doi.org/10.1016/j.jconrel.2019.05.037.

[21] F.P. Pons-Faudoa, et al., Changes in local tissue microenvironment in response to subcutaneous long-acting delivery of tenofovir alafenamide in rats and non-human primates, J. Contr. Release 358 (2023) 116–127.
[22] A. Fayzullin, A. Bakulina, K. Mikaelyan, A. Shekhter, A. Guller, Implantable drug delivery systems and foreign body reaction: traversing the current clinical landscape, Bioengineering 8 (2021) 205.
[23] T.D. Zaveri, et al., Contributions of surface topography and cytotoxicity to the macrophage response to zinc oxide nanorods, Biomaterials 31 (2010) 2999–3007, https://doi.org/10.1016/j.biomaterials.2009.12.055.
[24] J.C. Doloff, et al., The surface topography of silicone breast implants mediates the foreign body response in mice, rabbits and humans, Nat. Biomed. Eng. 1–16 (2021).
[25] M.E. Wiseman, C.W. Frank, Antibody adsorption and orientation on hydrophobic surfaces, Langmuir 28 (2012) 1765–1774.
[26] M.S. Birajdar, et al., Inhibition of capsular contracture of poly (dimethyl siloxane) medical implants by surface modification with itaconic acid conjugated gelatin, J. Ind. Eng. Chem. 89 (2020) 128–138.
[27] R. Shelton, A. Rasmussen, J. Davies, Protein adsorption at the interface between charged polymer substrata and migrating osteoblasts, Biomaterials 9 (1988) 24–29.
[28] Q. Yang, et al., Zwitterionic polymer coating suppresses microglial encapsulation to neural implants in vitro and in vivo, Advanced biosystems 4 (2020) 1900287.
[29] M. Viola, et al., Subcutaneous delivery of monoclonal antibodies: how do we get there? J. Contr. Release 286 (2018) 301–314.
[30] G. Shankar, et al., Assessment and reporting of the clinical immunogenicity of therapeutic proteins and peptides—harmonized terminology and tactical recommendations, AAPS J. 16 (2014) 658–673.
[31] A.S. De Groot, D.W. Scott, Immunogenicity of protein therapeutics, Trends Immunol. 28 (2007) 482–490.
[32] K.A. Connors, Chemical Kinetics: the Study of Reaction Rates in Solution, Wiley-VCH Verlag GmbH, 1990.
[33] Sage, D., Prodanov, D., Tinevez, J.-Y. & Schindelin, J.in ImageJ User & Developer Conference.
[34] J.S. Di Martino, et al., A tumor-derived type III collagen-rich ECM niche regulates tumor cell dormancy, Nature cancer 3 (2022) 90–107.
[35] C. Greiner, et al., Robust quantitative assessment of collagen fibers with picrosirius red stain and linearly polarized light as demonstrated on atherosclerotic plaque samples, PLoS One 16 (2021) e0248068.
[36] J. Liu, et al., Picrosirius-Polarization method for collagen fiber detection in tendons: a mini-review, Orthop. Surg. 13 (2021) 701–707.
[37] L. Rittié, Method for picrosirius red-polarization detection of collagen fibers in tissue sections, Fibrosis: methods and protocols 395–407 (2017).
[38] R. Rezakhaniha, et al., Experimental investigation of collagen waviness and orientation in the arterial adventitia using confocal laser scanning microscopy, Biomech. Model. Mechanobiol. 11 (2012) 461–473.
[39] Z. Püspöki, M. Storath, D. Sage, M. Unser, Transforms and operators for directional bioimage analysis: a survey, Focus on bio-image informatics (2016) 69–93.
[40] S. Capuani, et al., Localization of drug biodistribution in a 3D-bioengineered subcutaneous neovascularized microenvironment, Materials Today Bio 16 (2022) 100390.
[41] H.C. Liu, et al., Intratumoral nanofluidic system enhanced tumor biodistribution of PD-L1 antibody in triple-negative breast cancer, Bioengineering & Translational Medicine 8 (2023) e10594.
[42] R.C. Wood, E.L. LeCluyse, J.A. Fix, Assessment of a model for measuring drug diffusion through implant-generated fibrous capsule membranes, Biomaterials 16 (1995) 957–959.
[43] F.P. Pons-Faudoa, et al., Antiviral potency of long-acting islatravir subdermal implant in SHIV-infected macaques, J. Contr. Release 366 (2024) 18–27.
[44] D. Fine, et al., A robust nanofluidic membrane with tunable zero-order release for implantable dose specific drug delivery, Lab Chip 10 (2010) 3074–3083.
[45] L.-C. Xu, C.A. Siedlecki, Effects of surface wettability and contact time on protein adhesion to biomaterial surfaces, Biomaterials 28 (2007) 3273–3283.
[46] T.D. Ngo, A. Kashani, G. Imbalzano, K.T. Nguyen, D. Hui, Additive manufacturing (3D printing): a review of materials, methods, applications and challenges, Compos. B Eng. 143 (2018) 172–196.
[47] S. Capuani, G. Malgir, C.Y.X. Chua, A. Grattoni, Advanced strategies to thwart foreign body response to implantable devices, Bioengineering & Translational Medicine (2022) e10300, https://doi.org/10.1002/btm2.10300.
[48] B. Huzum, et al., Biocompatibility Assessment of Biomaterials Used in Orthopedic Devices: an Overview, vol. 22, Experimental and Therapeutic Medicine, 2021, pp. 1–9.
[49] E. Blanco, et al., Effect of fibrous capsule formation on doxorubicin distribution in radiofrequency ablated rat livers, J. Biomed. Mater. Res. Part A: An Official Journal of The Society for Biomaterials, The Japanese Society for Biomaterials, and The Australian Society for Biomaterials and the Korean Society for Biomaterials 69 (2004) 398–406.
[50] F.P. Pons-Faudoa, A. Ballerini, J. Sakamoto, A. Grattoni, Advanced implantable drug delivery technologies: transforming the clinical landscape of therapeutics for chronic diseases, Biomedical microdevices 21 (2019) 1–22.
[51] M.A. Booth, et al., Polycrystalline diamond coating on 3D printed titanium scaffolds: surface characterisation and foreign body response, Mater. Sci. Eng. C 130 (2021) 112467.
[52] F. Robotti, et al., A micron-scale surface topography design reducing cell adhesion to implanted materials, Sci. Rep. 8 (2018), https://doi.org/10.1038/s41598-018-29167-2, 10887-10887.
[53] O. Veiseh, et al., Size-and shape-dependent foreign body immune response to materials implanted in rodents and non-human primates, Nat. Mater. 14 (2015) 643–651.
[54] B.F. Matlaga, L.P. Yasenchak, T.N. Salthouse, Tissue response to implanted polymers: the significance of sample shape, J. Biomed. Mater. Res. 10 (1976) 391–397.
[55] D.J. Li, et al., Thickness of fibrous capsule after implantation of hydroxyapatite in subcutaneous tissue in rats, J. Biomed. Mater. Res.: An Official Journal of The Society for Biomaterials, The Japanese Society for Biomaterials, and The Australian Society for Biomaterials 45 (1999) 322–326.
[56] D. Akilbekova, K.M. Bratlie, Quantitative characterization of collagen in the fibrotic capsule surrounding implanted polymeric microparticles through second harmonic generation imaging, PLoS One 10 (2015) e0130386.
[57] K. Safferling, et al., Wound healing revised: a novel reepithelialization mechanism revealed by in vitro and in silico models, JCB (J. Cell Biol.) 203 (2013) 691–709.